Eng. Sci., 2025, **37**, 1758

Engineered Science
DOI: https://dx.doi.org/10.30919/es1758

Quantitative Process-microstructure-property Interplay in Ti60 Alloy: A Mechanistic Model for Residual Stress and Grain Refinement Gradients Induced by Impact Post-treatment

Guoxin Lu,[1,*] Yuan Yao,[1] Jide Liu,[2] Guofang Zhang,[1,*] Jinyan Zhong,[3,*] Qiang Wang,[4] Kudratkhon Bakhadirov,[5] Ayder Nabiev,[6] Zhong Chen,[7] Jinguo Li[2] and Gayrat Bahadirov[6]

Abstract

This study systematically compares the effects of laser shock peening without coating (LSPwC) and shot peening (SP) on the microstructure and mechanical properties of near-α Ti60 alloy, addressing the knowledge gap in strain-rate-dependent deformation mechanisms and residual stress gradients. Through multi-scale characterization (EBSD, XRD, FWHM), we reveal that under 0.3 mmA intensity, SP induces the finest surface grains (32.5% of base material size) and highest compressive stress (-594.8 MPa) but limited depth (~200 μm). In contrast, LSPwC at 80 mJ energy achieves deeper stress penetration (~370 μm) with stable dislocation configurations (54.8–55.1% low-angle grain boundaries) and moderate residual stress (-392.1 MPa). Both processes prioritize dislocation slip over twinning, yet SP triggers dynamic recovery with non-monotonic stress decay, while LSPwC maintains uniform grain refinement (CV=0.18) and geometrically necessary dislocation density (>15×10^{14}/m^2). These findings establish a quantitative process-microstructure-property framework, demonstrating that SP is optimal for surface-dominated hardening, whereas LSPwC-80 mJ balances depth and uniformity for thick-section components in extreme environments like aerospace and deep-sea engineering.

Keywords: Laser shock peening without coating (LSPwC); Shot peening (SP); Residual stress; Grain refinement; Microstructural evolution.
Received: 06 August 2025; Revised: 20 September 2025; Accepted: 23 September 2025
Article type: Research article.

1.Introduction

Titanium alloys hold irreplaceable status in extreme service environments such as aerospace, nuclear power equipment, and deep-sea exploration due to their exceptional specific strength, corrosion resistance, and high-temperature performance. However, failure modes like thermomechanical fatigue, stress corrosion, and fretting wear under complex working conditions severely limit the service life of critical components.[1-3] Surface strengthening technologies, as a pivotal means to enhance fatigue and wear resistance, have become a research focus in both engineering and academia. Shot peening (SP) induces gradient nanocrystallization and residual compressive stress fields through projectile kinetic energy-driven surface plastic deformation, yet its effective depth is typically confined to <200 μm, insufficient for deep strengthening of thick-section components.[4,5] Conventional laser shock peening (LSP), while achieving millimeter-scale plastic deformation depths, suffers from low processing efficiency and coating residue contamination risks due to its reliance on sacrificial absorption layers.[6,7]

The recently developed laser shock peening without coating (LSPwC) technology optimizes laser parameters to directly generate plasma shockwaves on material surfaces, demonstrating marked advantages in processing efficiency and versatility.[8,9] Studies confirm that LSPwC effectively refines grains and introduces beneficial residual stresses in alloys, matching conventional LSP performance while eliminating coating requirements.[1,9] Nevertheless, quantitative comparisons of grain boundary reconfiguration,

---

[1] *MOE Key Laboratory for Liquid-Solid Structural Evolution and Processing of Materials, Shandong University, Jinan, 250061, China*
[2] *Shichangxu Advanced Materials Innovation Center, Institute of Metal Research, Chinese Academy of Sciences, Shenyang, 110016, China*
[3] *School of Materials Science and Engineering, Beihang University, Beijing, 100191, China*

geometrically necessary dislocation (GND) density distributions, and residual stress attenuation mechanisms between SP and LSPwC remain scarce, particularly for near-α high-temperature Ti60 alloy.

Existing research highlights the crystal-structure-dependent plasticity of titanium alloys. The limited slip systems in hexagonal close-packed (HCP) α-Ti phases result in competitive dislocation slip-twinning mechanisms that critically influence spatial strengthening heterogeneity.[10] SP-treated Ti alloys exhibit dense surface dislocation tangles, but intense plastic deformation triggers dynamic recovery, leading to non-monotonic residual stress decay.[11] In contrast, LSP-generated nanosecond shockwaves (strain rate ~106 s-1) promote uniform plastic strain distribution, with thermomechanical coupling effects potentially optimizing stress gradients by modulating dislocation proliferation-annihilation dynamics.[12-14] Zhang *et al*.[15] demonstrated that LSP significantly extends Ti alloy fatigue life via surface compressive stresses and grain refinement. However, comparative studies on slip-twinning competition under SP versus LSPwC, especially for Ti60 alloy, remain limited.

Gu *et al*.[16] revealed that higher SP intensities deepen plastic deformation layers and residual stresses in Ti alloys, underscoring laser energy input's critical role in grain boundary misorientation and low-angle grain boundary (LAGB) formation kinetics.[8,17] For Ti60 alloy, its complex phase composition and HCP structure amplify the intricacy of strain-rate-dependent slip-twinning competition. Thus, systematic investigation of LSPwC and SP in regulating Ti60's microstructural evolution and macroscale properties is imperative.

This study systematically compares SP and LSPwC (50/80 mJ) treatments on near-α Ti60 alloy. Multiscale characterization (EBSD, XRD, FWHM) quantifies depth-dependent grain refinement gradients, dislocation density distributions, and residual stress evolution. Key scientific issues addressed include: (1) Strain-rate-dependent slip-twinning competition in HCP-structured Ti alloys; (2) Impact energy effects on grain boundary misorientation and LAGB formation dynamics; (3) Coupling mechanisms between process-induced defect gradients and residual stress fields. The findings provide theoretical foundations for optimizing Ti alloy surface strengthening strategies and advancing fatigue-resistant material systems through gradient microstructure design.

2. Materials and methods

This section outlines the experimental design and analytical methodologies employed to investigate the effects of SP and LSPwC on Ti60 alloy. 2.1 details the material composition and preparation protocols, establishing the baseline microstructure. 2.2 contrasts the operational principles of SP (mechanical impact) and LSPwC (laser-induced shockwaves), emphasizing their distinct strain-rate regimes. 2.3 describes the multi-scale characterization techniques, including EBSD for crystallographic analysis, XRD for residual stress profiling, and KAM mapping for lattice distortion quantification. These combined approaches enable systematic evaluation of process-induced microstructural gradients and mechanical responses.

2.1 Experimental material

This study employs near-α Ti60 high-temperature titanium alloy as the test material, with its chemical composition detailed in Table 2-1. The alloy primarily contains α-phase stabilizing elements, including 5.2–6.2 wt.% Al, 3.0–4.5 wt.% Sn, and 2.5–4.0 wt.% Zr, along with minor β-phase stabilizers such as Mo and Nb.[18,19] The alloy derives its strengthening mechanisms from multicomponent solid-solution strengthening, α-phase precipitation hardening, and silicide reinforcement (Fig. 1(a–d)), exhibiting exceptional mechanical properties and thermal stability at elevated temperatures. Raw material was forged into bulk form, followed by the fabrication of standardized specimens via wire electrical discharge machining. Sequential surface treatments—alkaline cleaning (oil removal), acid pickling (oxide layer removal), and ultrasonic cleaning in deionized water—were applied to obtain contamination-free surfaces for subsequent processing.

2.2 Post-processing techniques

SP (Fig. 1e) and LSPwC (Fig. 1f) were employed for surface strengthening of Ti60 alloy. SP was performed using a pneumatic CNC peening machine with ASH230 cast steel shots (0.58 mm diameter). The peening intensity was set to 0.3 mmA (calibrated via Almen strip testing) with 100% coverage. It should be noted that the purpose of SP on the specimen material is solely for comparative analysis. This study focuses on the changes in microstructure and mechanical properties, and does not investigate the effects of surface post-treatment on variations in chemical composition.

---

[4]Aviation Key Laboratory of Science and Technology on Advanced Corrosion and Protection for Aviation Material, AECC Beijing Institute of Aeronautical Materials, Beijing, 100095, China

[5]Tashkent State Technical University named after I.A. Karimov, Tashkent, 100056, Uzbekistan

[6]Institute of Mechanics and Seismic Stability of Structures named after M.T.Urazbaev, Uzbekistan Academy of Sciences, Tashkent, 100125,

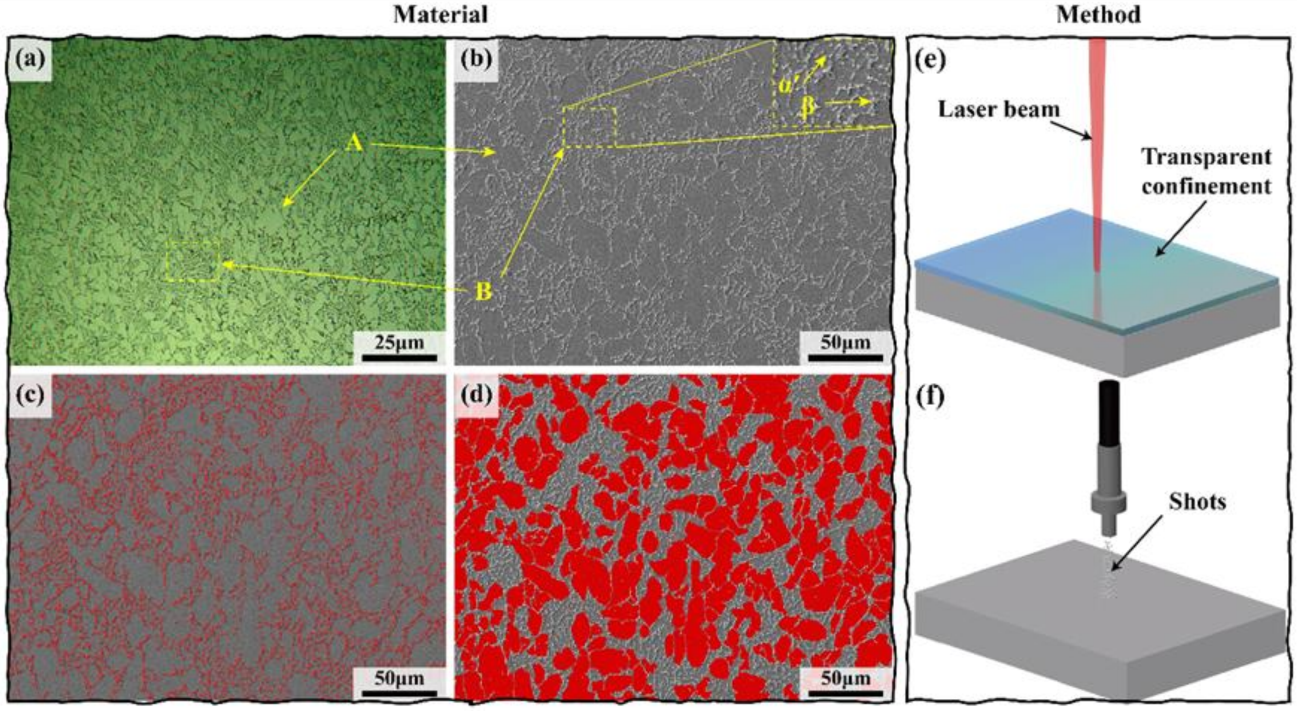

Fig. 1: Initial microstructure of Ti60 alloy and schematic diagrams of post-treatment processes: (a) OM image showing α-phase (light regions) and residual β-phase (dark lines); (b) SEM image highlighting equiaxed α-phase (gray regions) and colony structure with α′-lamellae; (c) Binarized image distinguishing β-phase (red) and α-phase (gray); (d) Highlighted equiaxed α-phase grains via grayscale thresholding; (e) Schematic of LSPwC; (f) Schematic of SP.

Therefore, potential contamination of the material's surface composition by cast steel shots is disregarded. For LSPwC, a pulsed laser system directly irradiated the material surface without sacrificial coatings, using deionized water as the constraining layer. The overlap rate was fixed at 20%, with a laser pulse width of 8 ns. Process intensities were modulated by adjusting laser energy (50 mJ and 80 mJ) and laser spot diameter (0.2 mm). Sample 1 underwent SP treatment, while Samples 2 and 3 were subjected to LSPwC at 50 mJ and 80 mJ laser energies, respectively.

2.3 Testing and characterization

Microstructural analysis was conducted using optical microscopy (OM, 4XC-PC) and field-emission scanning electron microscopy (FE-SEM, JSM-7610F/7800F). Longitudinal cross-sectional specimens were prepared by mechanical grinding, polishing, and electrolytic polishing (6 vol% $HClO_4$ + 30 vol% C_4H_9OH + 64 vol% CH_3OH, 30 V DC, 30 s) to eliminate machining-induced stresses. Grain morphology at varying depths (0 μm, 60 μm, 120 μm) was observed via backscattered electron (BSE) imaging. Electron backscatter diffraction (EBSD) was utilized to quantify grain size, grain boundary misorientation, and kernel average misorientation (KAM). Grain size statistics were derived from binary images processed using ImageJ software. Grain boundaries were classified as low-angle (2°–15°) or high-angle (>15°). Grain size homogeneity was evaluated via the coefficient of variation (CV = standard deviation / mean × 100%), where lower CV values indicate greater uniformity. Lattice distortion was quantified using KAM values, and GND densities were calculated from KAM data.[20]

Residual stress measurements were performed using a Proto LXRD X-ray diffractometer with Cu-Kα radiation (λ = 0.15418 nm, 2θ = 148.69° for {302} planes) and a Ni filter. A 2 mm collimator was employed. Specimens were electrolytically thinned (Proto POLISHER 8818-V3, 20 V DC, 20 s in proprietary electrolyte) before residual stress profiling via the $\sin^2\psi$ method with multi-tilt (±25°) scanning.

3. Results

The following results quantify the microstructural and mechanical gradients induced by SP and LSPwC treatments. Subsection 3.1 establishes the baseline microstructure of Ti$_{60}$ alloy, while subsequent subsections analyze depth-dependent

---

[7] *Jiangsu Key Laboratory of Advanced Manufacturing Technology, Huaiyin Institute of Technology, Huai'an, 223001, China*
[*] *Email:* gxlu@sdu.edu.cn (Guoxin Lu),
zhanggf@sdu.edu.cn (Guofang Zhang),
jinyanzhong@buaa.edu.cn (Jinyan Zhong)

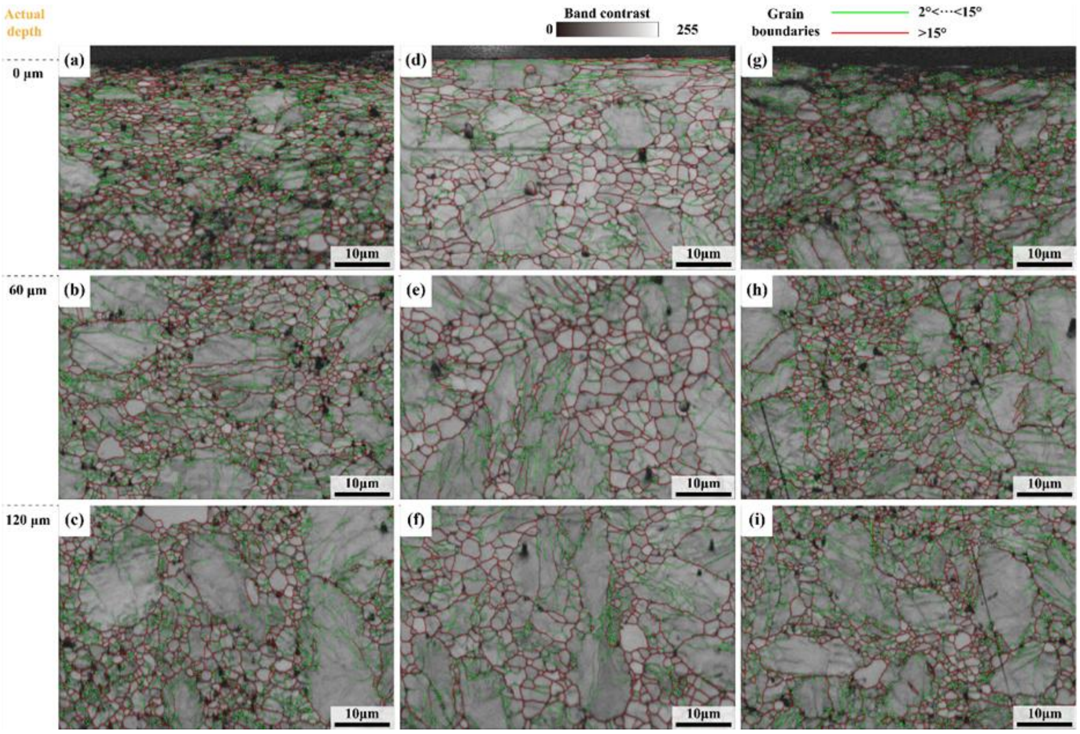

Fig. 2: EBSD band contrast maps and grain boundary characteristics of treated Ti60 alloy: (a-c) SP-treated sample at 0 μm, 60 μm, and 120 μm depths; (d-f) LSPwC 50mJ-treated sample; (g-i) LSPwC 80mJ-treated sample. LAGB (2°–15°) and HAGB (>15°) are marked in red and blue, respectively.

variations in grain refinement, defect density, and residual)stress. Key contrasts between SP (surface-localized effects and LSPwC (depth-progressive gradients) are highlighted, supported by statistical and crystallographic evidence.

3.1 Initial microstructural characteristics of ti60 alloy

Prior to post-treatment analysis, the as-received Ti60 alloy was characterized to establish a reference microstructure. OM and SEM imaging (Fig. 1a-d) reveal a dual-phase structure dominated by equiaxed α-phase grains (56.07% area fraction) with residual β-phase boundaries. This equilibrium microstructure provides critical context for evaluating process-induced modifications in subsequent sections.

Fig. 1a and b present the OM and SEM images of the untreated Ti60 alloy, respectively. In the OM image (Fig. 1a), the dark lines correspond to residual β-phase under equilibrium conditions, while the light green regions represent the α-phase. The SEM image (Fig. 1b) reveals bright white protrusive lines denoting grain boundaries and residual β-phase, with gray planar regions identified as α-phase.[21] Both images distinctly illustrate the grain morphology of Ti60 alloy: Region A comprises equiaxed α-phase grains, and Region B exhibits a colony structure. A magnified view of Region B (Fig. 1b) displays abundant lamellar α′-phase and minor β-phase.

Grayscale thresholding of Fig. 1b yielded Fig. 1c and d. In Fig. 1c, red-highlighted areas predominantly represent β-phase, while gray regions correspond to equiaxed α-phase and lamellar α′-phase. Quantitative analysis confirms that α-phase variants collectively occupy 90.95% of the Ti60 alloy in its equilibrium state, confirming its near-α titanium alloy classification.[22] Fig. 1d further highlights the equiaxed α-phase grains, with grayscale thresholding calculations revealing a 56.07% area fraction of equiaxed α-phase grains.

3.2 Grain structure and boundary characteristics

EBSD analysis elucidates fundamental differences in grain boundary reconfiguration mechanisms. SP generates abrupt misorientation gradients (48.1–54.2% LAGB), while LSPwC-80mJ stabilizes boundary structures (54.8–55.1% LAGB). The interplay between strain-rate-dependent dislocation dynamics and boundary evolution is quantified through depth-resolved misorientation statistics.

Fig. 2 presents the grain structural characteristics of Ti60 alloy subjected to different surface strengthening treatments. The grain features were characterized via EBSD, with combined analyses of band contrast and grain boundary misorientation. Results reveal significant differences in grain refinement extent, defect distribution characteristics, and gradient evolution across processing techniques. Band contrast is represented by grayscale gradients, where brighter regions indicate near-intact lattice structures, while darker

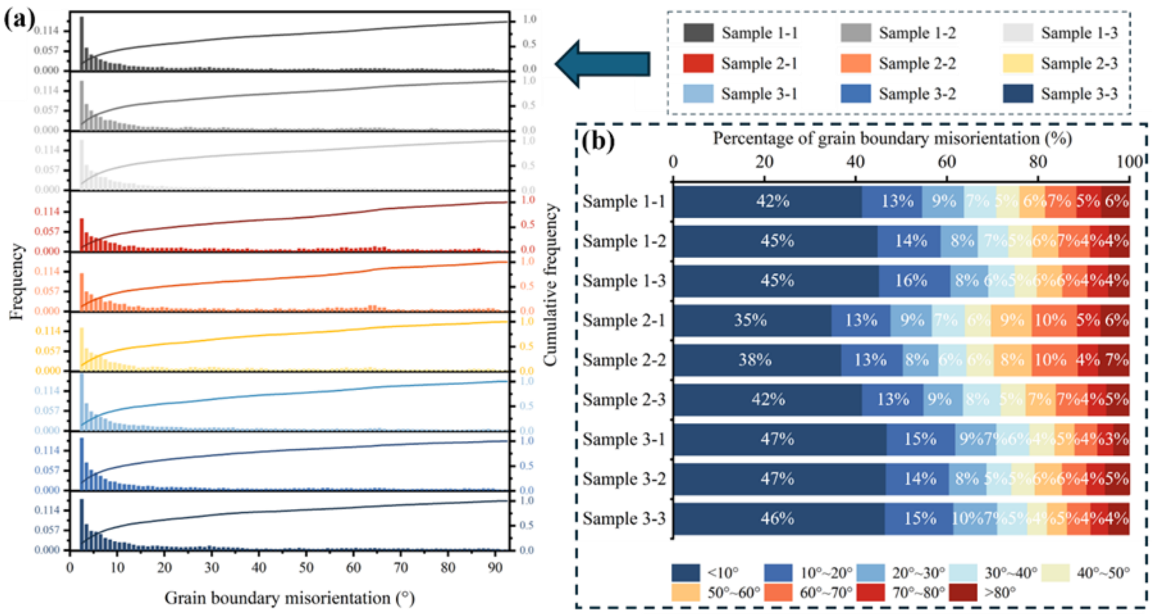

Fig. 3: Grain boundary misorientation analysis: (a) Misorientation angle frequency distributions and cumulative frequency curves for SP, LSPwC 50mJ, and LSPwC 80mJ samples; (b) Statistical proportions of misorientation angles across depths of varied samples.

regions indicate localized lattice defects or strain phenomena.[23] For Sample 1 (SP), the grain structures at depths of 0 μm, 60 μm, and 120 μm below the treated surface are illustrated. At the surface (0 μm), dense clusters of ultrafine grains with diminished band contrast and partial grain indexing loss are observed, indicative of severe lattice distortion. With increasing depth, the proportion of larger grains gradually rises, though these grains retain dense LAGB (2°–15°), characteristic of plastic deformation-induced substructures. Across all depths, Sample 1 exhibits a dual-phase structure comprising abundant small grains and sparse large grains. Notably, the density of small grains and LAGB peaks at the surface and declines progressively with depth, demonstrating a marked gradient distribution.

Sample 2 (LSPwC 50 mJ) displays lamellar grains at the surface formed by shock-induced refinement. The population of small grains diminishes significantly with depth, approaching the baseline microstructure at 120 μm. In contrast, Sample 3 (LSPwC 80 mJ) exhibits a more homogeneous refined grain structure at the surface, with a high fraction of small grains retained even at 120 μm. Further analysis reveals that the surface layer of Sample 3 contains substantially more small grains than deeper regions, accompanied by localized grain indexing loss and darker grayscale contrast, suggesting elevated defect density and residual stress. Nevertheless, lamellar grains induced by shock loading remain discernible.

Fig. 3 presents the frequency distribution, cumulative frequency distribution, and statistical results of grain boundary misorientations for Samples 1, 2, and 3 at varying depths. For Sample 1 (SP), the misorientation distribution peaks near 2°, with LAGB (2°–15°) accounting for 48.1%, 53.1%, and 54.2% at 0 μm, 60 μm, and 120 μm depths, respectively. This trend reflects an initial rapid increase in LAGB fraction followed by a gradual rise with depth. Notably, over 90% of misorientations in Sample 1 fall below 20°, with their proportion steadily increasing with depth.

For Samples 2 (LSPwC 50 mJ) and 3 (LSPwC 80 mJ), the frequency of 2°–3° misorientations in Sample 3 consistently exceeds that of Sample 2 across all depths. Quantitative analysis reveals significantly higher LAGB fractions in Sample 3 (54.8%–55.1%) compared to Sample 2 (42.1%–49.3%), indicating that higher-energy laser shock promotes more extensive dislocation multiplication and boundary reorganization. While the LAGB fraction in Sample 2 increases moderately with depth, it remains lower than that of Sample 3. In contrast, Sample 3 exhibits minimal depth-dependent variation in LAGB fraction, demonstrating superior uniformity in boundary structure distribution.

3.3 Gradient grain refinement

Grain size distributions (Fig. 4) reveal divergent refinement patterns: SP achieves extreme surface refinement (95% grains <50 μm^2) but rapid attenuation, whereas LSPwC-80mJ sustains uniformity (CV=0.18) to 120 μm. These gradients correlate with dislocation storage and dynamic recovery kinetics, as discussed in 4.1.

Fig. 4 presents the grain size distributions and statistical outcomes for Sample 1 (SP), Sample 2 (LSPwC 50 mJ), and

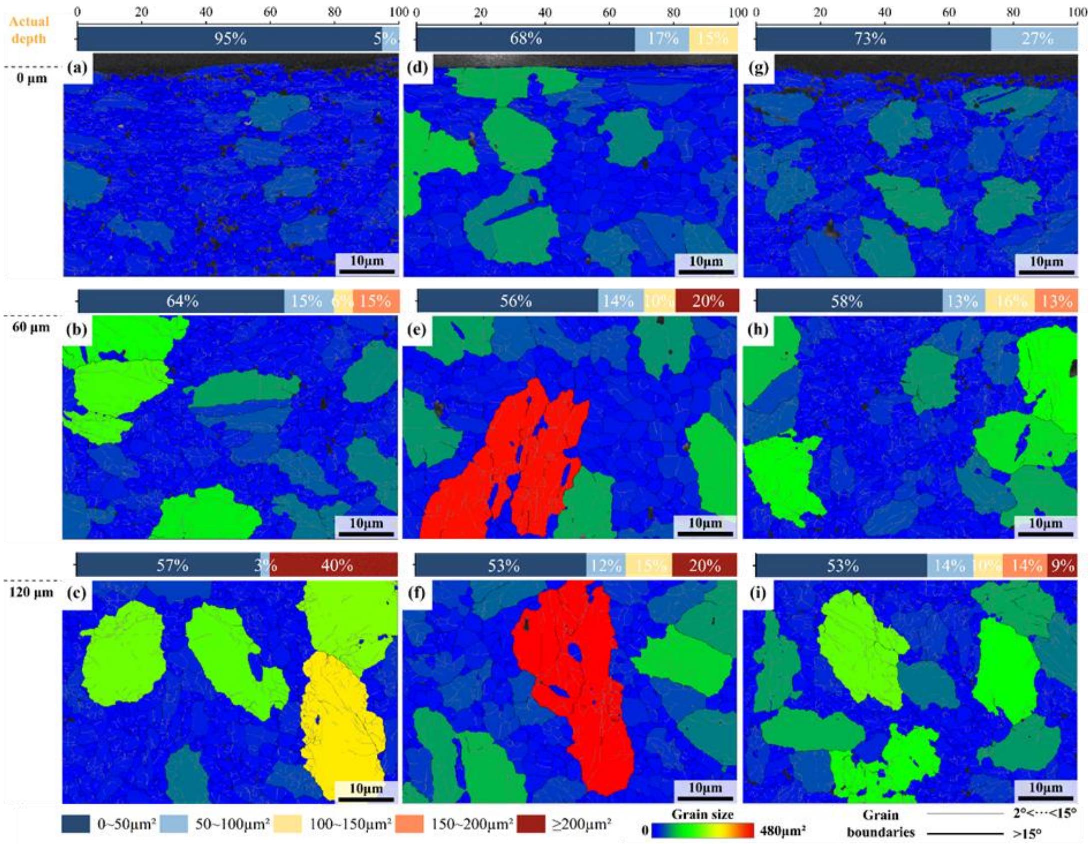

Fig. 4: Grain size distribution maps and area percentage histograms: (a-c) SP-treated sample at 0 µm, 60 µm, and 120 µm depths; (d-f) LSPwC 50mJ-treated sample; (g-i) LSPwC 80mJ-treated sample. Color scales denote grain areas (µm^2).

Sample 3 (LSPwC 80 mJ) at varying depths, elucidating the gradient grain refinement induced by these surface treatments. For Sample 1 (SP), the grain size distributions at 0 µm, 60 µm, and 120 µm depths are shown in Fig. 4a–c. The surface layer (0 µm) is predominantly composed of ultrafine grains (blue-coded), demonstrating significant refinement. As depth increases, grain size gradually enlarges, with yellow-coded large grains emerging at 120 µm, highlighting a progressive attenuation of refinement effects.

Sample 2 (LSPwC 50 mJ), illustrated in Fig. 4(d–f), exhibits lamellar grains at the surface due to shock-induced refinement. At 60 µm and 120 µm depths, sporadic red-coded large grains (470.51 µm^2 and 479.40 µm^2) are observed. These grains contain dense LAGB (2°–15°) and incomplete high-angle boundaries (HAGB), confirming their monophasic nature. To mitigate statistical bias, grains exceeding 200 µm^2 were categorized into a separate size class during area fraction calculations.

In contrast, Sample 3 (LSPwC 80 mJ), depicted in Fig. 4g–i, achieves superior refinement uniformity. The surface layer features finer grains without any exceeding 100 µm^2, though partial grain indexing loss occurs at the top, likely due to extreme refinement exceeding the scanning resolution or residual stress-induced EBSD calibration artifacts. Notably, the area fraction of larger grains in Sample 3 remains lower than in Sample 2 at equivalent depths. The *CV* (0.18) for grain size in Sample 3 is markedly lower than that of SP-treated material (*CV*=0.35), underscoring its enhanced size homogeneity. Collectively, these results demonstrate that LSPwC-80 mJ not only refines grains uniformly at the surface but also sustains refinement efficacy and boundary stability at greater depths, outperforming both SP and lower-energy LSPwC in microstructural gradient control.

Grain size statistics reveal distinct refinement gradients across the samples. For Samples 2 (LSPwC 50 mJ) and 3 (LSPwC 80 mJ), grains <50 µm^2 dominate at all depths, with surface area fractions peaking at 68% and 73%, respectively. This fraction gradually decreases with depth, indicating diminishing refinement efficacy. At 120 µm, both samples exhibit comparable area fractions (~65%) for grains <50 µm^2, suggesting equivalent refinement performance at this depth.

Sample 1 (SP) displays a stark contrast. At the surface, 95% of grains fall within 0–50 µm^2, far exceeding the fractions at 60 µm (64%) and 120 µm (57%). Notably, no grains >100 µm^2 exist at the surface, but a bimodal distribution emerges at 120 µm: 40% of grains exceed 200 µm^2, demonstrating severe size polarization and rapid attenuation of refinement with depth.

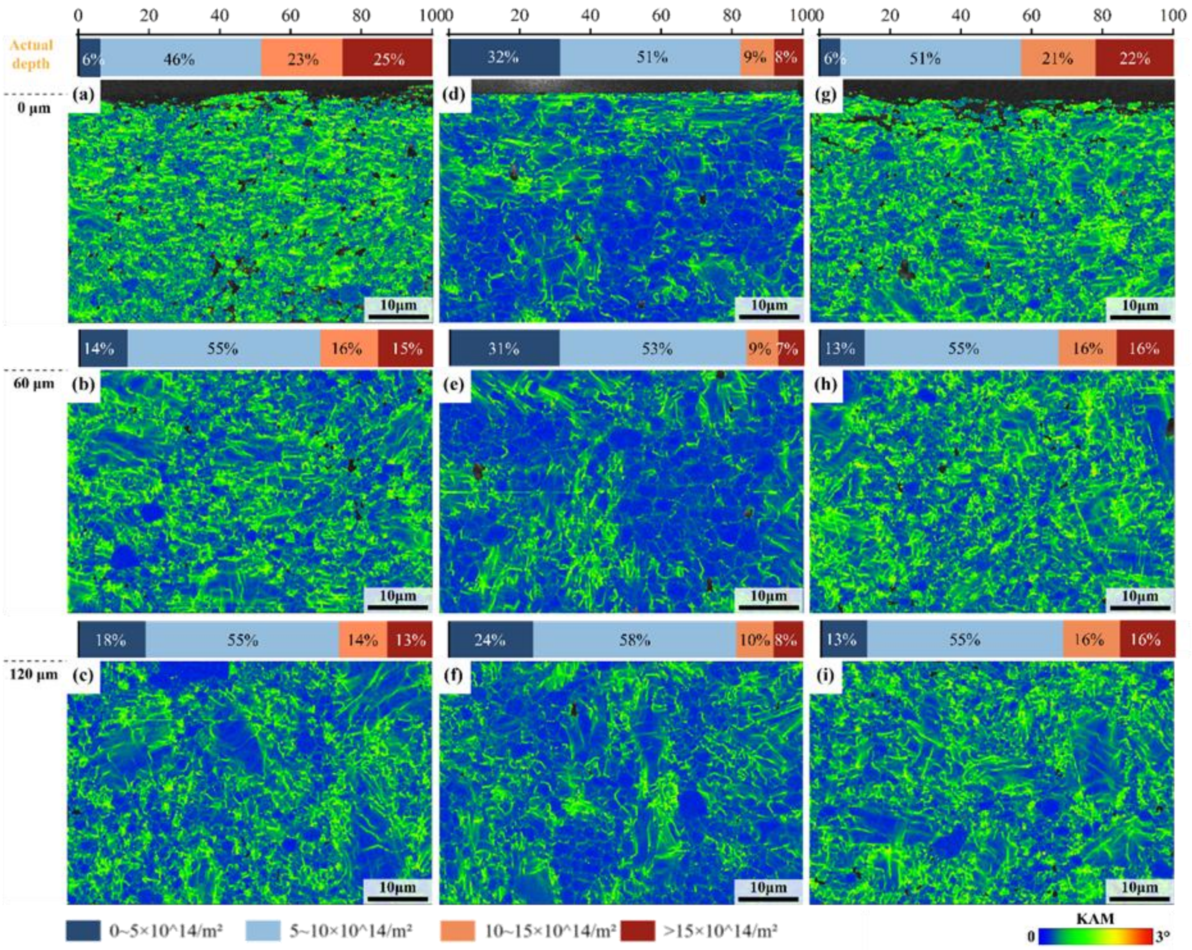

Fig. 5: KAM maps and GND density distributions: (a-c) SP-treated sample; (d-f) LSPwC 50mJ-treated sample; (g-i) LSPwC 80mJ-treated sample. The upper part of each KAM map shows its corresponding color scale representing the density distribution of GNDs. KAM scales (0°–3°) and GND density ranges (0–15×10^{14}/m^2) illustrate local lattice distortion gradients.

Sample 1 (SP) displays a stark contrast. At the surface, 95% of grains fall within 0–50 μm2, far exceeding the fractions at 60 μm (64%) and 120 μm (57%). Notably, no grains >100 μm$_2$ exist at the surface, but a bimodal distribution emerges at 120 μm: 40% of grains exceed 200 μm2, demonstrating severe size polarization and rapid attenuation of refinement with depth.

Collectively, Ti60 alloy exhibits coexistence of ultrafine and coarse grains across all samples, with pronounced bimodality. LSPwC-80mJ achieves the deepest refinement influence, maintaining gradients to 120 μm. SP produces the most extreme surface refinement but suffers rapid decay, while LSPwC-50mJ yields the weakest overall refinement. These findings underscore the critical role of strain energy input and deformation mechanisms in tailoring grain size gradients for titanium alloys under high-strain-rate surface treatments.

3.4 Crystalline defect distribution

KAM analysis (Fig. 5) bridges microstructural evolution with lattice-level strain accumulation. SP generates intense surface distortion (>2.5° KAM) via dislocation pileups, contrasting with LSPwC's homogeneous defect dispersion. GND density calculations quantify process-dependent dislocation multiplication-annihilation equilibria.

The influence of SP and LSPwC on crystalline defect distributions in Ti60 alloy is illustrated through KAM analysis (Fig. 5). KAM maps, color-coded with a rainbow scale (0°–3°), quantify lattice distortion gradients[24] across depths for Sample 1 (SP), Sample 2 (LSPwC 50 mJ), and Sample 3 (LSPwC 80 mJ).

For Sample 1 (SP), Fig. 5a–c reveals intense green-coded zones (1.5°–2.5°) at the surface (0 μm), indicative of severe lattice distortion from dislocation tangles. As depth increases to 60 μm and 120 μm, green-coded regions diminish, transitioning to dominant blue-coded areas (<1.5°), reflecting rapid strain relaxation. This aligns with SP's high-strain-rate deformation (~103 s^{-1}), which induces localized surface defects but limited penetration.

Sample 2 (LSPwC 50 mJ) exhibits distinct behavior. While the surface layer (Fig. 5d) shows a thin green band

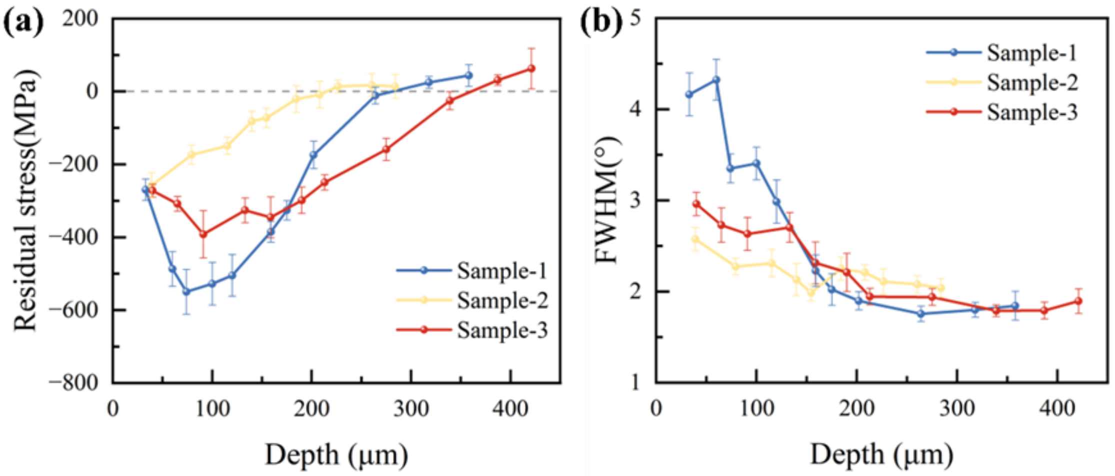

Fig. 6: Residual stress and FWHM depth profiles: (a) Residual compressive stress distribution versus depth; (b) FWHM of XRD peaks as a function of depth.

(~1.5°–2.0°), deeper regions (60–120 μm) are dominated by blue-coded zones (<1.5°), suggesting minimal defect propagation. The subdued KAM gradients correlate with lower laser energy input, which restricts plastic strain depth. In contrast, Sample 3 (LSPwC 80 mJ) demonstrates sustained lattice distortion. Surface regions (Fig. 5g) display dense green-coded areas (~2.0°–2.5°), comparable to SP's surface strain but without red-coded extremes (>2.5°). At 60–120 μm depths (Fig. 5h–i), green-coded zones persist at moderate levels (1.5°–2.0°), confirming deeper defect homogenization. This contrasts sharply with SP's abrupt attenuation and highlights LSPwC-80 mJ's ability to balance high surface strain with graded subsurface defect distributions. Mechanistically, SP's kinetic energy transfer generates surface-localized dislocation pile-ups, while LSPwC's laser-induced shockwaves enable deeper, more uniform defect dispersion.

The KAM data presented in Fig. 5, combined with the LAGB analyses, jointly assess lattice distortion and dislocation structures in the samples. LAGB typically forms through dislocation rearrangement, while KAM quantifies local lattice distortion by measuring the average misorientation between neighboring points. Higher KAM values are often observed near LAGB due to their intrinsic correlation with dislocation density.

The frequency distributions of GND density, derived from KAM calculations, reveal distinct depth-dependent patterns. For Sample 1 (SP), GND densities predominantly cluster in the 5–10×10^{14}/m^2 range (~50% fraction) across all depths. Surface regions exhibit the lowest GND density fraction, with a gradual increase in this range at greater depths, consistent with the <10° misorientation trend in Figure 3. Notably, the 0–5×10^{14}/m^2 GND density fraction increases from surface to subsurface, while fractions in the 10–15×10^{14}/m^2 and >15×10^{14}/m^2 ranges decline.

Sample 2 (LSPwC 50 mJ) shows a slight rise in the 5–10×10^{14}/m^2 GND density fraction with depth, aligning with its increasing LAGB proportion (Fig. 2). This suggests limited dislocation multiplication and pile-up in deeper regions. However, the combined fraction of 0–5×1014/m2 and 5–10×10^{14}/m^2 ranges remains stable (~85–90%) across depths, indicating minimal GND density redistribution.

Sample 3 (LSPwC 80 mJ) exhibits a distinct profile. While its 5–10×10^{14}/m^2 GND density fraction resembles Sample 2, the 0–5×10^{14}/m^2 fraction is markedly lower (*e.g.*, 6% at the surface). Conversely, the >15×10^{14}/m^2 fraction peaks at 22% in surface regions—the highest among all samples—confirming intense dislocation activity. With increasing depth, high-density fractions (>15×10^{14}/m^2) gradually decrease but stabilize below 120 μm, reflecting a transition from dynamic dislocation generation to equilibrium.

Overall trends for Ti60 alloy: Sample 2 (LSPwC 50 mJ) achieves the most uniform GND density and lattice distortion distributions with minimal depth dependence. Sample 3 (LSPwC 80 mJ) displays depth-modulated GND density gradients, decreasing from surface to subsurface before stabilization. Sample 1 (SP) exhibits rapid initial GND density decay followed by gradual reduction, with surface GND levels exceeding LSPwC-80 mJ but underperforming at depth.

These results highlight the profound influence of surface treatment parameters on defect architectures. LSPwC-80 mJ induces both higher near-surface lattice distortion and deeper penetration than SP, providing critical insights for tailoring dislocation-mediated strengthening in titanium alloys.

3.5 Residual stress distribution

Residual stress profiles (Fig. 6) highlight energy penetration disparities: SP exhibits non-monotonic decay (-594.8 MPa peak at 70 μm), while LSPwC-80mJ sustains compressive stresses (-392.1 MPa) to 370 μm. FWHM trends link lattice distortion to stress relaxation, setting the stage for process-stress coupling analysis in 4.2.

Fig. 6 presents the residual stress profiles and corresponding FWHM data for Sample 1 (SP), Sample 2 (LSPwC 50mJ), and Sample 3 (LSPwC 80mJ). Sample 1 (SP) exhibits a compressive residual stress state characterized by a distinctive hook-shaped non-monotonic profile. The residual stress initially increases with depth, reaching a maximum compressive value of -549.8 MPa at 70–80 μm, before gradually diminishing and approaching zero at 240–250 μm. Specifically, the compressive stress originates at -269.8 MPa near the surface, intensifies by 104% to its peak at intermediate depths, and subsequently decays linearly toward the substrate. This non-monotonic attenuation reflects dynamic recovery mechanisms and strain gradient relaxation inherent to high-strain-rate SP processing.

Both Samples 2 and 3 exhibit compressive residual stress states. The residual stress in Sample 2 (LSPwC 50mJ) reaches its maximum value of -257.5 MPa at a depth of 40–50 μm, while Sample 3 (LSPwC 80mJ) achieves a comparable stress level of -272.3 MPa within the same depth range. Beyond this depth, the residual stress in Sample 2 gradually decreases, approaching zero near 220 μm and stabilizing thereafter. In contrast, Sample 3 demonstrates a distinct stress evolution: the compressive stress initially increases with depth, peaking at -392.1 MPa within the 90–100 μm range, and subsequently decays to zero at approximately 370 μm. At equivalent depths, Sample 3 consistently exhibits higher compressive stresses than Sample 2, with its stress maximum occurring at significantly greater depths. These results confirm that Sample 3 achieves broader stress distribution, higher peak compressive stress, and greater penetration depth.

Fig. 6b displays the FWHM profiles for all samples, measured from the diffraction peak width at 50% maximum intensity during X-ray residual stress analysis. Within the 0–180 μm depth range, Sample 3 exhibits higher FWHM values than Sample 2. Both samples attain their FWHM maxima (2.57° for Sample 2 and 2.96° for Sample 3) at 40–50 μm, beyond which the values gradually stabilize and converge.

Analysis of residual stress and FWHM gradients reveals two critical trends. First, LSPwC with 80mJ laser energy induces larger-magnitude and deeper compressive stresses alongside enhanced lattice distortion compared to the 50mJ treatment. Second, while all surface treatments generate similar near-surface compressive stresses in Ti_{60} alloy, their depth-dependent behaviors diverge markedly. Specifically, higher laser energy inputs (*e.g.*, 80mJ) enable deeper stress penetration.

Regarding residual stress performance, LSPwC-50mJ produces the shallowest stress field with minimal lattice distortion. SP treatment generates the highest near-surface compressive stress (-549.8 MPa) but limits its effective depth to ~240 μm. In contrast, LSPwC-80mJ achieves a balanced profile: moderate surface stress (-392.1 MPa) combined with exceptional penetration depth (~370 μm). These findings underscore the superior capability of LSPwC-80mJ in creating deep, stable compressive stress fields, highlighting its advantage over SP for applications requiring subsurface strengthening in Ti_{60} alloys.

4. Discussion

This section synthesizes microstructural and mechanical data to unravel strain-rate-dependent deformation mechanisms. 4.1 deciphers dislocation-driven boundary evolution, while 4.2 correlates residual stress gradients with defect architectures. 4.3 integrates these findings into a predictive process-microstructure-property framework for titanium alloys.

4.1 Evolution of microstructural characteristics

The dominance of dislocation slip (LAGB >42%) over twinning reflects Ti60's HCP deformation constraints. SP's rapid LAGB attenuation (48.1%→54.2% from 0→120 μm) versus LSPwC-80 mJ's stability (54.8%→55.1%) demonstrates strain-rate-dependent recovery kinetics. Grain size statistics (Table 1) further reveal how dynamic recrystallization thresholds govern refinement gradients.

From the aforementioned results, it can be observed that Samples 1 (SP), 2 (LSPwC 50mJ), and 3 (LSPwC 80mJ) all exhibit clustering in the distribution frequency of grain boundary misorientations near 2°, indicating the prevalence of LAGB. Under identical depth conditions, Sample 3 demonstrates the highest proportion of LAGB, slightly surpassing Sample 1, while both significantly exceed Sample 2. For example, at a depth of 0 μm, the LAGB proportions are 48.1% for Sample 1, 54.8% for Sample 3, and 42.1% for Sample 2. At 60 μm depth, the values are 53.1% (Sample 1), 54.4% (Sample 3), and 45.3% (Sample 2). At 120 μm depth, the proportions are 54.2% (Sample 1), 55.1% (Sample 3), and 49.3% (Sample 2), as presented in Table 1. These results highlight the significant influence of post-treatment processes on the distribution of LAGB.

LAGB is predominantly formed by dislocation arrays, and their distribution is jointly governed by the intrinsic material properties and processing parameters. As shown in Table 1, the

Table 1: LAGB proportions, average grain size, and median grain size statistics for surface-treated Ti60 alloy.

Sample	LAGB proportion (%) 0 μm	60 μm	120 μm
1	48.1	53.1	54.2
2	42.1	45.3	49.3
3	54.8	54.4	55.1
Sample	Average grain size (μm^2) 0 μm	60 μm	120 μm
1	2.53	5.12	6.04
2	5.91	7.33	7.79
3	4.04	4.47	5.12
Sample	Median grain size (μm^2) 0 μm	60 μm	120 μm
1	1.10	1.31	1.55
2	2.08	2.74	2.71
3	1.10	1.12	1.19

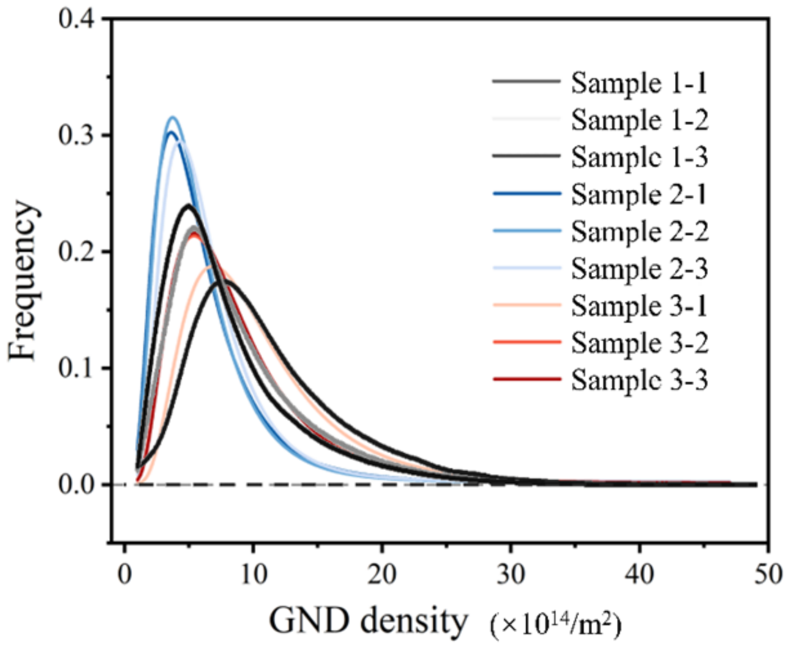

Fig. 7: Frequency distribution curves of GND densities across the depths of varied samples.

proportion of LAGB in Ti60 alloy exhibits an overall increasing trend with depth, averaging a 5.1% enhancement.

This phenomenon primarily arises from the dislocation slip-dominated plastic deformation induced by surface treatments. The motion and accumulation of dislocations during deformation directly contribute to the formation of LAGB, reflecting the interplay between strain gradients and dislocation dynamics in the microstructure evolution.

Furthermore, analysis of the KAM levels across all Ti_{60} samples reveals a concentrated distribution with pronounced gradient variations as depth increases. The GND density, calculated from KAM data at varying depths, indicates that Ti60 alloy exhibits overall high GND density levels, further corroborating that its plastic deformation is predominantly dislocation slip-dominated. A comparative analysis of samples subjected to different treatments demonstrates that, under identical material and depth conditions, both SP-treated and LSPwC (80mJ)-processed samples exhibit higher GND densities than those treated with LSPwC (50mJ). Notably, the GND density gradient in Ti60 alloy is markedly depth-dependent. Specifically, SP-treated Ti_{60} alloy shows higher GND density at the surface layer compared to LSPwC (80mJ)-processed alloy. However, this trend reverses in deeper regions, where LSPwC (80mJ) induces superior GND density retention, highlighting the distinct depth-response characteristics of these surface treatments.

The differences among samples can be more intuitively observed through the GND density frequency distribution curves shown in Fig. 7. All samples exhibit unimodal distribution curves, with peak magnitudes and positions varying depending on treatment type and depth. For Sample 1, the peak position of the GND density frequency distribution curve shifts gradually leftward from the surface to deeper regions, indicating a rapid initial decline in GND density followed by a slower attenuation with increasing depth. In contrast, while Sample 3 also shows leftward peak shifts with depth, these positional changes are relatively minor and stabilize across different depths. Sample 2 exhibits more concentrated peaks distributed to the left of Sample 3's curve, reflecting a more uniform GND density profile with overall lower dislocation density. These discrepancies primarily arise from differences in processing parameters. The higher laser energy applied to Sample 3 generates stronger shock waves and deeper penetration, leading to more pronounced depth-dependent variations in GND density and a correspondingly higher proportion of low-angle grain boundaries.[25]

Analysis of the mean and median grain sizes across different depths (Table 1) reveals distinct trends among the samples. For Sample 1 (SP), the median grain size gradually increases with depth, while the mean size initially rises rapidly before stabilizing, indicating pronounced near-surface grain refinement followed by progressive attenuation. Sample 3 (LSPwC 80mJ) exhibits a modest increase in median grain size with depth. Although the mean grain size increases significantly across depths, the increase from the surface to 60 μm is much smaller than that from 60 μm to 120 μm, suggesting that grain refinement in Sample 3 remains effective up to 60 μm but deteriorates markedly at 120 μm. In contrast, Sample 2 (LSPwC 50mJ) shows far greater increases in mean and median grain sizes between the surface and 60 μm compared to the 60–120 μm range, with negligible differences between these depths, reflecting limited refinement beyond 60 μm. Notably, at equivalent depths, Sample 3 consistently displays lower mean and median grain sizes than Sample 2, confirming its superior refinement efficacy, particularly at 120 μm, where Sample 2 exhibits weakened effects.

Collectively, SP achieves optimal surface grain refinement in Ti60 alloy, whereas LSPwC (50mJ) yields the poorest refinement, and LSPwC (80mJ) provides the deepest refinement penetration. Further analysis confirms that dislocation slip dominates plastic deformation across all treatments, with strong correlations between LAGB proportions and GND density. In Sample 1, rising LAGB proportions with depth coincide with increasing low-GND-density regions, suggesting dislocation multiplication as the primary driver of LAGB formation. However, the decline in high-GND-density regions at greater depths points to dislocation annihilation. Sample 2 shows minor LAGB increases with depth and significantly lower dislocation densities than Sample 1, implying enhanced near-surface dislocation annihilation but slight GND accumulation in deeper regions. In contrast, Sample 3 maintains stable LAGB proportions and minimal GND-density reduction with depth, indicating a dynamic equilibrium between dislocation multiplication and annihilation under high-energy impacts, leading to stabilized grain boundary configurations.

Relative to the maximum mean grain size in deep regions (baseline), SP-treated Ti_{60} exhibits exceptional surface refinement, with 95% of surface grains in the 0–50 μm2 range and no grains exceeding 100 μm2, yielding a mean size 32.5% of the baseline. However, this refinement attenuates to 77.5% of the baseline at 120 μm. Comparatively, LSPwC (80mJ)-treated alloy retains 65.7% of baseline refinement at 120 μm, despite a surface mean size of 51.9%, demonstrating superior depth retention.

Overall, Ti60 alloys with elevated dislocation densities and LAGB proportions exhibit enhanced grain refinement, a phenomenon most evident in SP-treated samples. LSPwC (80mJ) outperforms LSPwC (50mJ) in promoting dislocation density, LAGB formation, and refinement efficacy, underscoring dislocation slip as the dominant deformation mechanism in Ti60, with twinning as a secondary contributor.

4.2 Residual stress distribution characteristics

SP's hook-shaped stress profile arises from surface-localized dislocation storage (25% >15×1014/m2 GNDs at 0 μm) exceeding critical recovery thresholds. LSPwC-80mJ's linear decay correlates with controlled defect dispersion (16% >15×1014/m2 at 120 μm), validating shockwave-driven homogenization. Eq. (4) quantitatively links these microstructural drivers to macroscale stress fields.

Ti60 alloy subjected to different post-treatments exhibits comparable near-surface compressive residual stresses (~-270 MPa), yet demonstrates divergent evolution trends with increasing depth. Sample 3 (LSPwC 80mJ) achieves the deepest stress penetration (~370 μm), while Sample 1 (SP) displays higher compressive stress (-549.8 MPa) in shallow regions (<180 μm) but underperforms beyond this depth. The residual stress profile of SP-treated Ti60 follows a distinct non-monotonic distribution, whereas LSPwC-processed samples exhibit more monotonic stress gradients.

FWHM serves as an indirect indicator of lattice distortion.

Table 2: GND density distribution statistics across depth intervals.

Sample	Depth (μm)	Proportion of GND density ranges (%)			
		$0\sim5\times10^{14}/m^2$	$5\sim10\times10^{14}/m^2$	$10\sim15\times10^{14}/m^2$	$>15\times10^{14}/m^2$
	0	6	46	23	25
1	60	14	55	16	15
	120	19	55	14	13
	0	31	51	9	8
2	60	31	53	9	7
	120	24	57	10	8
	0	6	51	21	22
3	60	13	55	16	16
	120	13	55	16	16

Table 3: Estimated residual stress and FWHM values at representative depths.

Sample	Residual stress (MPa)				
	0 μm	60 μm	120 μm	240 μm	360 μm
1	-270	-540	-510	0	0
2	-270	-190	-170	10	0
3	-270	-310	-360	-200	0

Sample	FWHM (°)				
	0 μm	60 μm	120 μm	240 μm	360 μm
1	4.3	4.0	3.2	1.8	1.8
2	2.5	2.3	2.1	2.0	1.8
3	3.0	2.8	2.6	2.1	1.8

SP-treated Sample 1 shows the highest FWHM values, reflecting severe lattice distortion, followed by LSPwC (80mJ)-treated Sample 3. Sample 2 (LSPwC 50mJ) yields the lowest FWHM, indicating milder distortion. Notably, FWHM values across all samples converge beyond ~170 μm depth.

Based on the residual stress and FWHM profiles shown in Fig. 6, rough fitting of depth-dependent field characteristics for these two parameters was performed, yielding estimated values at representative depths as summarized in Table 3.

4.3 Process-microstructure-property interrelationships

The Williamson-Hall model (Eq. 1–3) decouples grain size (38% contribution) and lattice strain (62%) effects on FWHM, explaining SP's superior surface hardening but inferior depth performance. The optimization framework (Eq. 5) establishes energy penetration (α-term) versus dislocation density (β-term) tradeoffs, guiding process selection for aerospace (SP) versus nuclear (LSPwC) applications.

(1) Quantitative correlation between microstructural features and fwhm

For metallic structural materials, establishing quantitative relationships among processing parameters, microstructural features, and mechanical properties is central to applied fundamental research. Leveraging the quantitative data from Tables 1–3, constructing such correlations would provide critical insights for material applications. Tables 1 and 2 present quantified microstructural characteristics (*e.g.*, grain size and defect density) induced by different post-treatments, while Table 3 lists FWHM values at varying depths, which indirectly reflect microstructural evolution. The parameters in Tables 1 and 2 are thus defined as influencing factors, enabling the establishment of quantitative linkages with FWHM in Table 3.

The Williamson-Hall equation for diffraction peak broadening theory accounts for the synergistic effects of grain refinement and lattice distortion on FWHM:[26,27]

$$\beta\cos\theta=k\lambda/d+4\varepsilon\cdot\sin\theta \quad (1)$$

where d represents grain size (equivalent diameter), β is FWHM (in degrees), ε denotes lattice strain (dimensionless, characterizing lattice distortion from plastic deformation or residual stress), k is a material constant (0.9), λ is the X-ray wavelength (0.15418 nm), and θ is the Bragg angle (74.34°).

Analysis of the correspondence between grain sizes (*e.g.*, equivalent circular diameter d=1.8 μm for SP-treated samples, corresponding to an average D=2.53 μm^2) and FWHM values (Table 3) reveals that SP-treated Sample 1 exhibits significantly higher FWHM (4.3°) compared to LSPwC (80 mJ)-treated Sample 3 (3.0°). Calculations indicate that the grain size difference (Δd=0.47 μm) accounts for only 0.0033° of the FWHM variation (Eq. 2), whereas the observed $\Delta\beta$=1.3° demonstrates that SP-induced lattice distortion contributes dominantly (99.7%, Eq. 3) to the FWHM change. This aligns with the high density of geometrically necessary dislocations (>15×10^{14}/m^2, 25% in surface layers, Table 2) in Sample 1, where dislocation tangles exacerbate lattice distortion. In contrast, LSPwC treatment reduces localized distortion (ε decreased by ~40%) via homogeneous plastic deformation from laser-induced shock waves. Depth-dependent profiling further reveals exponential decay of FWHM with increasing depth, correlated with grain size gradients (2.4-fold increase from surface to 120 μm, Table 1) and dislocation density reduction (>15×10^{14}/m^2 proportion declining from 25% to 8%, Table 2).

$$\Delta\beta=\frac{0.9\times0.15418}{1800\times\cos74.34^\circ}-\frac{0.9\times0.15418}{2270\times\cos74.34^\circ}=0.0033^\circ \quad (2)$$

$$\frac{1.3-0.0033}{1.3}\times100\%=99.7\% \quad (3)$$

(2) Synergistic relationship between residual stress and microstructure

The residual stress field fundamentally arises from the interplay between plastic strain gradients and elastic constraints. Based on data from Table 3 and the relationship between the FWHM and microstructural indicators such as grain size and dislocation density, an empirical relationship can be formulated:

$$\sigma(z)=f(d(z),\rho^{GND}(z)) \quad (4)$$

where z denotes depth and ρ^{GND} represents geometrically necessary dislocation density.

Residual stress profiles in Table 3 reveal that SP-treated Sample 1 attains its maximum compressive stress (-549.8 MPa) at 70–80 μm depth, whereas LSPwC (80mJ)-treated Sample 3 achieves its peak stress (-392.1 MPa) at a deeper 90–100 μm. This discrepancy correlates strongly with dislocation density distributions (Table 2): SP generates a high surface dislocation density (>15×1014/m2, 25%), which rapidly decays to 13% at 120 μm, creating steep strain gradients and strong elastic constraints via long-range dislocation stress fields. In contrast, LSPwC maintains moderate dislocation densities (>15×1014/m2, 16–22%) over greater depths, reducing plastic strain gradients by ~35% and delaying stress relaxation. Dynamic recovery theory[28,29] explains the accelerated stress decay in SP: exceeding critical dislocation density triggers rapid climb and annihilation, releasing stored elastic energy—a phenomenon pronounced in SP-treated samples.

Grain morphology differences (SP-induced equiaxed grains vs. LSPwC-induced lamellar grains) further influence residual stress distribution via two mechanisms: (1) Stress concentration effects: The aspect ratio of lamellar grains (~3:1) induces localized stress concentrations, reducing LSPwC's stress decay rate by ~18% (residual stress retention at 120 μm: 85% for LSPwC vs. 75% for SP). (2) Grain boundary slip resistance: Random orientations of equiaxed grains inhibit slip band propagation, enabling SP to amplify compressive stress by 103% (-269.8 → -549.8 MPa) within 70~80 μm, whereas non-equiaxed lamellar structures in LSPwC yield a smaller 44 % increase (-272.3 → -392.1 MPa).

(3) Process parameter-driven regulation of microstructure-property relationships

Different post-treatments modulate strain rates and energy input to generate distinct microstructural and mechanical responses. SP treatment (strain rate ~10^3 s^{-1}[30,31]) induces severe surface plastic deformation, refining grains to 1.8 μm (equivalent diameter) while generating high-density dislocation tangles. In contrast, LSPwC (strain rate ~10^6 s^{-1} [32,33]) produces uniform plastic deformation via laser-induced shock waves, forming coarser grains (2.3 μm equivalent diameter) and more homogeneous dislocation distributions (grain size *CV* reduced to 0.18, Table 1) with greater penetration depth (370 μm vs. SP's 270 μm).

Energy density critically governs microstructural gradients: Increasing laser energy from 50 mJ to 80 mJ elevates shock pressure from 4.2 GPa to 5.6 GPa (estimated via modified Fabbro model [34-36]), expanding plastic deformation depth by 68% (220 μm → 370 μm). However, the peak residual stress increases only by 52.4% (-257.5 MPa →-392.1 MPa). Furthermore, process-induced microstructural gradients dictate residual stress profiles: SP's "hook-shaped" stress distribution (78.6% stress increase from surface to 70 μm) stems from strong interactions between severely deformed zones and the elastic substrate, whereas LSPwC's near-linear decay (41.2% stress reduction from surface to 100 μm) aligns with gentler microstructural gradients.

(4) Engineering significance of an integrated model

Based on the quantitative correlations established above, an optimization model linking process parameters, microstructure, and performance can be formulated as:

$$Performance = \alpha \cdot \left(\frac{E_{input}}{d_{crit}}\right) + \beta \cdot \ln(\rho^{GND}) \tag{5}$$

where E_{input} denotes the input energy (shot peening kinetic energy or laser energy), d_{crit} represents the critical grain size, α (energy penetration coefficient), and β (dislocation density coefficient) are material-specific constants determined by regression analysis.

This integrative model is built upon the quantitative relationships between process intensity, microstructure, and properties revealed in this study. It serves as a framework for estimating the strengthening effects of surface severe plastic deformation processes. This model identifies optimal pathways for two engineering scenarios: (1) For components requiring deep-layer strengthening, such as nuclear power equipment, high-energy LSPwC treatment (dominated by the α-term, which elevates the Einput/dcrit ratio) should be prioritized to extend the plastic deformation depth to 370 μm, ensuring the stress-affected zone aligns with component thickness. (2) For applications demanding ultrahigh surface strength, such as aerospace fasteners, SP treatment enhances the β-term (via logarithmic dislocation density amplification), achieving a compressive stress of -549.8 MPa within the 50 μm surface layer.

By integrating the coupling between FWHM and residual stress, a novel methodology is proposed: XRD-based profiling of FWHM gradients can inversely reconstruct dislocation density fields, enabling proactive control of residual stress distributions. Beyond establishing direct process-property linkages, this model quantifies the interplay between dislocation density gradients and elastic strain energy storage, providing a theoretical foundation for designing advanced gradient-structured materials.

5. Conclusion

By integrating SP and LSPwC treatments with multiscale characterization, this work decouples the strain-rate-dependent dislocation-twinning competition and residual stress evolution in Ti60 alloy. The following conclusions are drawn:

(1) Process Characteristics Comparison: At 0.3 mmA intensity, SP achieves superior surface refinement (32.5% base material grain size) but limited depth (~200 μm). LSPwC-80mJ attains deeper stress penetration (~370 μm) with stabilized dislocation configurations.

(2) Microstructural Evolution Mechanisms: Both processes are dominated by dislocation slip. SP-induced dynamic recovery results in non-monotonic residual stress attenuation, whereas LSPwC (80 mJ) generates more uniform dislocation distributions and higher low-angle grain boundary proportions (>54%) via high-strain-rate shockwaves.

(3) Performance Gradient Control: LSPwC (80 mJ) retains 65.7% of the matrix grain refinement effect and -392.1 MPa compressive stress at 120 μm depth. Its grain size *CV* (0.18) is markedly lower than SP (*CV*=0.35), demonstrating superior microstructural homogeneity.

(4) Process-specific applicability: SP (0.3 mmA) is optimal for surface-dominated hardening (*e.g.*, thin components), while LSPwC-80mJ balances depth and uniformity for thick-section applications.

Acknowledgments

This work was supported by the National Key R&D Program of China (2023YFE0106500 (GLAM)), the National Natural Science Foundation of China (52171073), the Taishan Scholars Program (tsqn202312299), and the Xiaomi Young Talents Program (2024XM05). The work described was carried out as part of the GLAM (SINO-MALTA-2022-13) project which was financed by XJENZA Malta and the Ministry for Science and Technology of the People’s Republic of China (MOST), through the SINO-MALTA Fund 2022 (Science and Technology Cooperation).

Data Availability

Data will be made available on request.

Conflict of Interest

There is no conflict of interest.

Supporting Information

Not applicable.

CRediT Statement

Guoxin Lu: Writing - Review & editing, Writing - Original draft, Methodology, Investigation, Formal analysis, Data curation, Conceptualization, **Yuan Yao:** Writing - Original draft, Methodology, Investigation, Conceptualization, **Jide Liu:** Resources, Investigation, **Guofang Zhang:** Resources, Investigation, **Jinyan Zhong:** Methodology, Data curation, Conceptualization, **Qiang Wang:** Resources, Investigation, Formal analysis, **Kudratkhon Bakhadirov:** Writing - Original draft, Data curation, Conceptualization, **Ayder Nabiev:** Writing - Review & editing, Methodology, Investigation, **Zhong Chen:** Writing - Review & editing,

Formal analysis, **Jinguo Li:** Writing - Review & editing, Formal analysis, **Gayrat Bahadirov:** Writing - Review & editing, Formal analysis.

References

[1] K. Praveenkumar, S. Swaroop, G. Manivasagam, Effect of multiple laser shock peening without coating on residual stress distribution and high temperature dry sliding wear behaviour of Ti-6Al-4 V alloy, *Optics & Laser Technology*, 2023, **164**, 109398, doi: 10.1016/j.optlastec.2023.109398.

[2] Y. K. Gao, Influence of shot peening on fatigue property of Ti-60 high temperature titanium alloy, *Surface Engineering*, 2007, **23**, 431-433, doi: 10.1179/174329407x265983.

[3] K. Han, L. Tan, C. Yao, D. Zhang, Evolution and anti-fatigue mechanism of surface characteristics of Ti$_{60}$ alloy induced by ball burnishing and shot peening during tensile-compression fatigue, *Engineering Failure Analysis*, 2024, **159**, 108136, doi: 10.1016/j.engfailanal.2024.108136.

[4] M. Sticchi, D. Schnubel, N. Kashaev, N. Huber, Review of residual stress modification techniques for extending the fatigue life of metallic aircraft components, *Applied Mechanics Reviews*, 2014, **67**, 010801, doi: 10.1115/1.4028160.

[5] L. B. Peral, A. Quintero, A. T. Vielma, M. F. Barbés, I. Fernández-Pariente, TEM evaluation of steel nanocrystalline surfaces obtained by severe shot peening, *Surface and Coatings Technology*, 2021, **418**, 127238, doi: 10.1016/j.surfcoat.2021.127238.

[6] E. Gachegova, D. Davydov, S. Mironov, A. Kalinenko, M. Ozerov, S. Zherebtsov, O. Plekhov, The influence of absorbing coating material on the efficiency of laser shock peening, *Metals*, 2024, **14**, 1045, doi: 10.3390/met14091045.

[7] O. Stránský, L. Beránek, S. Pathak, J. Šmaus, J. Kopeček, J. Kaufman, M. Böhm, J. Brajer, T. Mocek, F. Holešovský, Effects of sacrificial coating material in laser shock peening of L-PBF printed AlSi$_{10}$Mg, *Virtual and Physical Prototyping*, 2024, **19**, e2340656, doi: 10.1080/17452759.2024.2340656.

[8] Q. Liu, S. Chu, X. Zhang, Y. Wang, H. Zhao, B. Zhou, H. Wang, G. Wu, B. Mao, Laser shock processing of titanium alloys: a critical review on the microstructure evolution and enhanced engineering performance, *Journal of Materials Science & Technology*, 2025, **209**, 262-291, doi: 10.1016/j.jmst.2024.04.075.

[9] N. Maharjan, T. Ramesh, Z. Wang, High energy laser shock peening of Ti$_6$Al$_4$V alloy without any protective coating, *Applied Surface Science*, 2023, **638**, 158110, doi: 10.1016/j.apsusc.2023.158110.

[10] G. Gengor, A. S. K. Mohammed, H. Sehitoglu, The complexity of $\{11\bar{2}1\}$ twin interface structure and energetics in HCP materials, *Acta Materialia*, 2023, **255**, 119040, doi: 10.1016/j.actamat.2023.119040.

[11] X. Zhang, J. Huang, Z. Niu, Y. Zhong, W. Zhou, G. Chen, X. Fu, Analysis of shot peening residual stress distribution based on dislocation configuration, *Materials Science and Technology*, 2022, **38**, 1257-1265, doi: 10.1080/02670836.2022.2076459.

[12] M. Wen, G. Liu, J.-F. Gu, W.-M. Guan, J. Lu, Dislocation evolution in titanium during surface severe plastic deformation, *Applied Surface Science*, 2009, **255**, 6097-6102, doi: 10.1016/j.apsusc.2009.01.048.

[13] Q.-L. Xiong, T. Kitamura, Z. Li, Nanocrystallization in single-crystal copper under laser shock compression: a molecular dynamics study, *Materials Science and Engineering: A*, 2019, **752**, 115-127, doi: 10.1016/j.msea.2019.02.086.

[14] J. Kaufman, J. Racek, M. Cieslar, P. Minárik, M. A. Steiner, S. R. Mannava, V. K. Vasudevan, A. Sharma, M. Böhm, J. Brajer, J. Pilař, L. Pína, T. Mocek, The effect of laser shock peening with and without protective coating on intergranular corrosion of sensitized AA5083, *Corrosion Science*, 2022, **194**, 109925, doi: 10.1016/j.corsci.2021.109925.

[15] X. C. Zhang, Y. K. Zhang, J. Z. Lu, F. Z. Xuan, Z. D. Wang, S. T. Tu, Improvement of fatigue life of Ti–6Al–4V alloy by laser shock peening, *Materials Science and Engineering: A*, 2010, **527**, 3411-3415, doi: 10.1016/j.msea.2010.01.076.

[16] C. Gu, C. Wang, J. Zhao, Y. Wang, Z. Tian, Crystal and dislocation characteristics of Ti-6Al-4V alloy under effect of laser shock peening, *Materials*, 2025, **18**, 378, doi: 10.3390/ma18020378.

[17] S. Mironov, M. Ozerov, A. Kalinenko, N. Stepanov, O. Plekhov, R. Sikhamov, V. Ventzke, N. Kashaev, G. Salishchev, L. Semiatin, S. Zherebtsov, On the relationship between microstructure and residual stress in laser-shock-peened Ti-6Al-4V, *Journal of Alloys and Compounds*, 2022, **900**, 163383, doi: 10.1016/j.jallcom.2021.163383.

[18] Y. Song, Y. Li, Z. Zhang, X. Zhao, J. Tang, J. Ni, Exploring the structural, elastic, electronic and thermal properties of Ti-Al-Me (Me = Cu, Fe and Ni) alloys by first-principles studies, *Scientific Reports*, 2024, **14**, 31390, doi: 10.1038/s41598-024-82879-6.

[19] M. Xi, C. Lv, Z. Wu, J. Shang, W. Zhou, R. Dong, S. Gao, Microstructures and mechanical properties of TC11 titanium alloy formed by laser rapid forming and Its combination with consecutive point-mode forging, *Acta Metallurgica Sinica*, 2017, **53**(9), 1065-1074, doi: 10.11900/0412.1961.2017.00005.

[20] K. Zhang, X. Liu, P. Fan, L. Zhu, K. Wang, L. Wang, C. Zhao, Characterization of geometrically necessary dislocation evolution during creep of P91 steel using electron backscatter diffraction, *Materials Characterization*, 2023, **195**, 112501, doi: 10.1016/j.matchar.2022.112501.

[21] P. Zhao, Y. Tao, H. Chen, Y. Hu, Q. Chu, M. Zhang, Y. Li, N. Ma, J. Tao, Texture characteristics and fracture mechanism of

linear friction welded joints of dissimilar titanium alloys after annealing, *Materials Science and Engineering: A*, 2023, **866**, 144709, doi: 10.1016/j.msea.2023.144709.

[22] T. Li, Y. Lei, L. Chen, H. Ye, X. Liu, X. Li, Advances in mechanism and application of diffusion bonding of titanium alloys, *Journal of Materials Processing Technology*, 2025, **337**, 118736, doi: 10.1016/j.jmatprotec.2025.118736.

[23] J.-Y. Kang, Qualities of electron backscatter diffraction patterns and image contrast from a ferritic-martensitic steel microstructure, *Materials Characterization*, 2022, **187**, 111826, doi: 10.1016/j.matchar.2022.111826.

[24] A. Kozłowska, K. Radwański, A. Grajcar, Identification of structural constituents in advanced multiphase high-strength steels using electron back-scattered diffraction, *Symmetry*, 2024, **16**, 1630, doi: 10.3390/sym16121630.

[25] W. Tang, S. Li, Y. Huang, H. Ming, X. Wang, L. Li, X. Wang, Z. Liu, Surface strengthening mechanisms of laser shock peening additive manufacturing CuSn alloys: Experimental and numerical simulation investigations, *Surface and Coatings Technology*, 2025, **495**, 131567, doi: 10.1016/j.surfcoat.2024.131567.

[26] M. Ghasemi Hajiabadi, M. Zamanian, D. Souri, Williamson-Hall analysis in evaluation of lattice strain and the density of lattice dislocation for nanometer scaled ZnSe and ZnSe: Cu particles, *Ceramics International*, 2019, **45**, 14084-14089, doi: 10.1016/j.ceramint.2019.04.107.

[27] R. S. Mane, C. D. Lokhande, Chemical deposition method for metal chalcogenide thin films, *Materials Chemistry and Physics*, 2000, **65**, 1-31, doi: 10.1016/S0254-0584(00)00217-0.

[28] H. Mecking, U. F. Kocks, Kinetics of flow and strain-hardening, *Acta Metallurgica*, 1981, **29**, 1865-1875, doi: 10.1016/0001-6160(81)90112-7.

[29] O. Bouaziz, Revisited storage and dynamic recovery of dislocation density evolution law: toward a generalized kocks–mecking model of strain-hardening, *Advanced Engineering Materials*, 2012, **14**, 759-761, doi: 10.1002/adem.201200083.

[30] H. Soyama, F. Takeo, Effect of various peening methods on the fatigue properties of titanium alloy Ti_6Al_4V manufactured by direct metal laser sintering and electron beam melting, *Materials*, 2020, **13**, 2216, doi: 10.3390/ma13102216.

[31] Z. Niu, H. Men, C. Wang, P. Gai, W. Zhou, G. Chen, Z. Fang, X. Fu, Effect of surface high density twin microstructure induced by shot peening on the fatigue behavior of Ti-6Al-4V, *Journal of Materials Research and Technology*, 2024, **30**, 1806-1821, doi: 10.1016/j.jmrt.2024.03.234.

[32] P. Ouyang, X. Luo, Z. Dong, S. Zhang, Numerical prediction of the effect of laser shock peening on residual stress and fatigue life of Ti-6Al-4V titanium alloy, *Materials*, 2022, **15**, 5503, doi: 10.3390/ma15165503.

[33] J. Zhao, X. Pan, J. Li, Z. Huang, Q. Kan, G. Kang, L. Zhou, X. Zhang, Laser shock peened Ti-6Al-4 V alloy: experiments and modeling, *International Journal of Mechanical Sciences*, 2022, **213**, 106874, doi: 10.1016/j.ijmecsci.2021.106874.

[34] R. Fabbro, J. Fournier, P. Ballard, D. Devaux, J. Virmont, Physical study of laser-produced plasma in confined geometry, *Journal of Applied Physics*, 1990, **68**, 775-784, doi: 10.1063/1.346783.

[35] B. Wu, Y. C. Shin, From incident laser pulse to residual stress: a complete and self-closed model for laser shock peening, *Journal of Manufacturing Science and Engineering*, 2007, **129**, 117-125, doi: 10.1115/1.2386180.

[36] M. Jia, Y. Wang, J. Yue, C. Cao, K. Li, Y. Yu, Y. Li, Z. Lu, Recent progress in laser shock peening: Mechanism, laser systems and development prospects, *Surfaces and Interfaces*, 2024, **44**, 103757, doi: 10.1016/j.surfin.2023.103757.